Engineering Fracture Mechanics 120 (2014) 26–42

Contents lists available at ScienceDirect

Engineering Fracture Mechanics

journal homepage: www.elsevier.com/locate/engfracmech

Implementation and verification of the Park–Paulino–Roesler cohesive zone model in 3D

Albert Cerrone [a,*], Paul Wawrzynek [a], Aida Nonn [b], Glaucio H. Paulino [c], Anthony Ingraffea [a]

[a] School of Civil and Environmental Engineering, Cornell University, 642 Rhodes Hall, Ithaca, NY 14853, USA
[b] Salzgitter Mannesmann Forschung GmbH, Ehinger Strasse 200, 47259 Duisburg, Germany
[c] Department of Civil and Environmental Engineering, University of Illinois at Urbana Champaign, 205 North Mathews Ave., Urbana, IL 61801, USA

ARTICLE INFO

Article history:
Received 3 August 2013
Received in revised form 19 December 2013
Accepted 12 March 2014

Keywords:
Cohesive zone modeling
Cohesive element
Intergranular fracture
Finite element analysis
PPR potential-based model

ABSTRACT

The Park–Paulino–Roesler (PPR) potential-based model is a cohesive constitutive model formulated to be consistent under a high degree of mode-mixity. Herein, the PPR's generalization to three-dimensions is detailed, its implementation in a finite element framework is discussed, and its use in single-core and high performance computing (HPC) applications is demonstrated. The PPR model is shown to be an effective constitutive model to account for crack nucleation and propagation in a variety of applications including adhesives, composites, linepipe steel, and microstructures.

1. Introduction and motivation

Cohesive zone modeling of fracture processes dates to Dugdale's strip yield model [1]. In this model, yield magnitude closure stresses are applied between the actual crack tip and a notional crack tip, the length of the total plastic zone, to circumvent the unrealistic prediction of infinite stresses at the crack tip. Barenblatt [2] placed material-specific stresses according to a prescribed distribution in the aforementioned inelastic zone, leading to the many cohesive zone models (CZMs) available today. Applications of CZMs abound in the literature. Hillerborg et al. [3] were the first to model failure in a material by adapting a CZM into a finite element analysis. The cohesive finite element method (CFEM) has been used to conduct studies across a wide range of material systems: rock (e.g. Boone et al. [4]), ductile materials at the microscale (e.g. Needleman [5] and Iesulauro [6]), ductile materials at the macroscale (e.g. Tvergaard and Hutchinson [7] and Scheider and Brocks [8]), concrete (e.g. Ingraffea et al. [9]; Elices et al. [10]; Park et al. [11]), bone (e.g. Tomar [12] and Ural and Vashishth [13]), functionally graded materials (Zhang and Paulino [14]), and asphalt pavements (Song et al. [15]). Hui et al. [16] and Park and Paulino [17] have presented a review of the literature in the field and thus the reader is referred to these articles and the references therein.

The fracture behavior in potential-based cohesive zone models is characterized by a potential function, from which traction–separation behavior proceeds. Taking the first derivative of this potential function with respect to the displacement separation, results in the cohesive tractions. The second derivative, in turn, provides the material tangent modulus. A cursory search of potential-based CZMs in the literature will undoubtedly return hundreds of models. Needleman's potential from

* Corresponding author. Tel.: +1 707 338 6304.
E-mail address: arc247@cornell.edu (A. Cerrone).

http://dx.doi.org/10.1016/j.engfracmech.2014.03.010
0013-7944/

Nomenclature

$\mathbf{B}$	strain-displacement matrix
E	Young's modulus
$\mathbf{D}$	material tangent stiffness matrix
D	coupled damage parameter
$\mathbf{f}$	internal force vector
$\mathbf{J}$	Jacobian
$\mathbf{K}$	stiffness matrix
K	strength coefficient
m, n	non-dimensional exponents
N_1, N_2, N_3, N_4	shape functions for 8-noded cohesive element
n, $t1$, $t2$	opening and sliding directions
$\mathbf{t}$	traction vector
T_n	normal cohesive traction
T_t	effective tangential cohesive traction
T_{t1}, T_{t2}	tangential cohesive tractions in sliding directions
$T_{max\ coupled}$	coupled cohesive strength
α, β	shape parameters
Γ_n, Γ_t	energy constants
Δ_n	normal separation
Δ_t	effective sliding displacement
Δ_{t1}, Δ_{t2}	sliding displacements
Δ_n^{max}, Δ_t^{max}	max normal and tangential separations reached during loading/unloading
δ_n, δ_t	normal and tangential final crack opening widths
δ_{nc}, δ_{tc}	normal and tangential critical opening displacements at which T_n and T_t equal σ_{max} and τ_{max}, respectively
$\bar{\delta}_n$, $\bar{\delta}_t$	normal and tangential conjugate final crack opening widths
ε_p	plastic strain
λ_n, λ_t	initial slope indicators
ν	Poisson's ratio
ξ, η	natural coordinate system axes
σ_{max}, τ_{max}	normal and tangential cohesive strengths
ϕ_n, ϕ_t	fracture energies
Ψ	PPR model's potential function
$\langle\cdot\rangle$	Macaulay bracket $\langle x\rangle = \begin{cases} 0, x < 0 \\ x, x \geq 0 \end{cases}$

1987 [5], often cited in the literature, describes the normal, Mode I, interaction with a polynomial potential; however, it is limited because it only considers decohesion by normal separation. Tvergaard extended Needleman's potential to better account for mode-mixity with the use of an interaction formula defining an effective displacement [18]. Needleman later developed a potential accounting for debonding by tangential separation [19] whereby the normal and tangential interactions are described by exponential and periodic functions, respectively. Alternatively, Xu and Needleman developed a potential where the normal and tangential separations are both described by exponential functions [20].

Park et al. published a unified potential-based CZM, the PPR (Park–Paulino–Roesler) CZM [21], that addresses the shortcomings of the prevailing potential-based CZMs in the literature, particularly with respect to mode-mixity, user flexibility, and consistency. First, it characterizes different fracture energies and cohesive strengths in each fracture mode, an accommodation not made by most CZMs. Moreover, it provides for several material failure behaviors by allowing the modeler to define the shape of the softening curve in both the normal and shear traction–separation relations; in most CZMs, softening behavior is hard-coded and cannot be changed. Finally, and perhaps most important, it is consistent in anisotropic fracture energy conditions; it demonstrates a monotonic change of the work-of-separation for both proportional and non-proportional paths of separation, a quality not seen in most CZMs.

This paper describes the generalization of the PPR model to three dimensions, details its implementation in a finite element framework, and presents its use in single-core and high performance computing (HPC) applications. We identify a variety of examples which assess the various features of the PPR model considering different loading conditions (e.g. quasi-static and dynamic), mode-mixity, bulk material behavior, and interfacial behavior (investigating the parameter space that defines the traction–separation relationship). The examples include a mode I T-peel specimen, a mixed-mode (I and II) bending specimen, an edge crack torsion (ECT) specimen (modes II and III), the Battelle Drop-Weight Tear (BDWT) test, and intergranular fracture (grain-boundary decohesion) at the microstructural scale.

2. Implementation

A description of the PPR's implementation and verification in two-dimensions can be found in Park et al. [21]. The generalization of the intrinsic PPR model to three-dimensions is discussed here.

2.1. Brief overview

Fig. 1 gives an overview of the cohesive interactions of the PPR model. The normal cohesive interaction region is rectangular and bounded by δ_n and $\bar{\delta}_t$. Complete cohesive normal failure occurs when the normal separation, Δ_n, reaches the normal final crack opening width, δ_n, or the effective sliding displacement, Δ_t, reaches the tangential conjugate final crack opening width, $\bar{\delta}_t$. The tangential cohesive interaction, in turn, is rectangular and bounded by δ_t and $\bar{\delta}_n$. Complete cohesive tangential failure occurs when the effective sliding displacement reaches the tangential final crack opening width, δ_t, or normal separation reaches the normal conjugate final crack opening width, $\bar{\delta}_n$.

The shape parameters α and β control the normal and tangential softening curve shapes. A shape parameter less than 2 causes plateau-type behavior, whereas a shape parameter greater than 2 yields behavior indicative of quasi-brittle materials.

When Δ_n reaches the critical opening displacement, δ_{nc}, the normal cohesive traction is at its maximum, σ_{max} (the normal cohesive strength). When the sliding displacement reaches the critical sliding displacement, δ_{tc}, the effective tangential traction is at its maximum, τ_{max} (the tangential cohesive strength). The area under the normal cohesive interaction for $\Delta_t = 0$ corresponds to the normal fracture energy, ϕ_n, while the area under the tangential cohesive interaction for $\Delta_n = 0$ corresponds to the tangential fracture energy, ϕ_t.

The three cohesive tractions T_n, T_{t1}, and T_{t2} are dependent upon the normal separation, Δ_n, and two sliding displacements, Δ_{t1} and Δ_{t2}. Fig. 2 illustrates these displacements.

The effective sliding displacement, Δ_t, is given by

$$\Delta_t = \sqrt{(\Delta_{t1})^2 + (\Delta_{t2})^2} \tag{1}$$

The tangential cohesive tractions, T_{t1} and T_{t2}, relate to Δ_t as follows:

$$\begin{aligned} T_{t1}(\Delta_n, \Delta_t, \Delta_{t1}) &= \frac{\Delta_{t1}}{\Delta_t} T_t(\Delta_n, \Delta_t) \\ T_{t2}(\Delta_n, \Delta_t, \Delta_{t2}) &= \frac{\Delta_{t2}}{\Delta_t} T_t(\Delta_n, \Delta_t) \end{aligned} \tag{2}$$

where T_t is an effective tangential traction formulated in the next section.

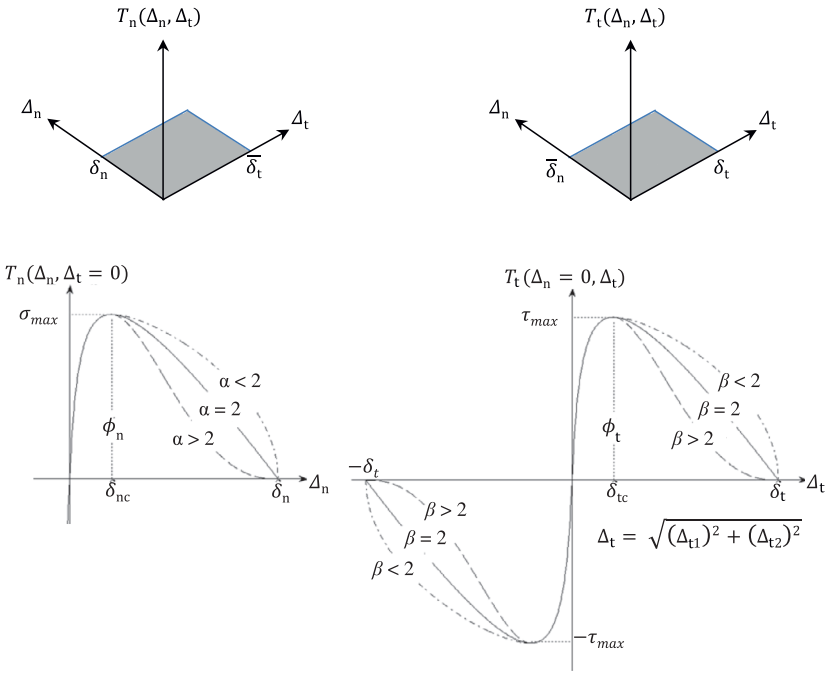

Fig. 1. Traction–separation relation of the PPR model.

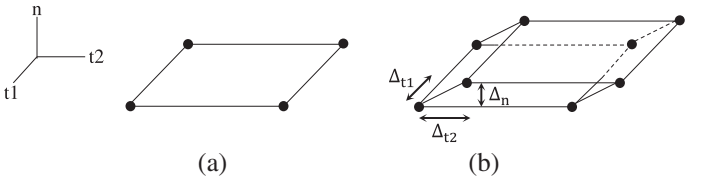

Fig. 2. Cohesive element collapsed (a) and deformed (b) with separations demarcated.

2.2. Expressions for the cohesive tractions

The PPR model is a function of four basic independent parameters in the normal and shearing fracture modes, namely cohesive strength, fracture energy, shape of softening curve, and initial slope of the traction–separation relationship. The potential, Ψ, is given by:

$$\Psi(\Delta_n,\Delta_{t1},\Delta_{t2}) = \min(\phi_n,\phi_t) + \left[\Gamma_n\left(1-\frac{\Delta_n}{\delta_n}\right)^{\alpha}\left(\frac{m}{\alpha}+\frac{\Delta_n}{\delta_n}\right)^{m} + \langle\phi_n-\phi_t\rangle\right] \times\left[\Gamma_t\left(1-\frac{\sqrt{(\Delta_{t1})^2+(\Delta_{t2})^2}}{\delta_t}\right)^{\beta}\left(\frac{n}{\beta}+\frac{\sqrt{(\Delta_{t1})^2+(\Delta_{t2})^2}}{\delta_t}\right)^{n} + \langle\phi_t-\phi_n\rangle\right] \tag{3}$$

As a matter of notation, the energy constants are Γ_n and Γ_t; the fracture energies are ϕ_n and ϕ_t; the non-dimensional exponents are m and n; the shape parameters are α and β; the final crack opening widths are δ_n and δ_t; the normal cohesive separation is Δ_n; and the effective sliding displacement is Δ_t. Note that $\langle\cdot\rangle$ is the Macaulay bracket, where $\langle x\rangle = \begin{cases} 0, x<0 \\ x, x\geq 0 \end{cases}$.

The energy constants Γ_n and Γ_t are given by:

$$\Gamma_n = \begin{cases} \left(\frac{\alpha}{m}\right)^m, & \phi_n < \phi_t \\ -\phi_n\left(\frac{\alpha}{m}\right)^m, & \phi_n \geqslant \phi_t \end{cases} \qquad \Gamma_t = \begin{cases} \left(\frac{\beta}{n}\right)^n, & \phi_t \leqslant \phi_n \\ (-\phi_t)\left(\frac{\beta}{n}\right)^n, & \phi_t > \phi_n \end{cases} \tag{4}$$

The non-dimensional exponents m and n are functions of the shape parameters and initial slope indicators, λ_n and λ_t, as:

$$m = \frac{\alpha(\alpha-1)\lambda_n^2}{1-\alpha\lambda_n^2}, \quad n = \frac{\beta(\beta-1)\lambda_t^2}{1-\beta\lambda_t^2} \tag{5}$$

$$\lambda_n = \frac{\delta_{nc}}{\delta_n}, \quad \lambda_t = \frac{\delta_{tc}}{\delta_t} \tag{6}$$

The initial slope indicators are measures of cohesive stiffness and control cohesive elastic behavior. Smaller initial slope indicators cause higher cohesive stiffness, which in turn decrease artificial elastic deformation. They are functions of δ_{nc} and δ_{tc}, the normal and tangential critical crack opening widths, respectively, corresponding to maximum normal and tangential cohesive strength, and δ_n and δ_t, the normal and tangential final crack opening widths, respectively, given by the expressions:

$$\delta_n = \frac{\phi_n}{\sigma_{max}}\alpha\lambda_n(1-\lambda_n)^{\alpha-1}\left(\frac{\alpha}{m}+1\right)\left(\frac{\alpha}{m}\lambda_n+1\right)^{m-1}$$
$$\delta_t = \frac{\phi_t}{\tau_{max}}\beta\lambda_t(1-\lambda_t)^{\beta-1}\left(\frac{\beta}{n}+1\right)\left(\frac{\beta}{n}\lambda_t+1\right)^{n-1} \tag{7}$$

Taking the gradient of the potential Ψ yields the normal and effective tangential cohesive tractions T_n and T_t, respectively. They are given below:

$$T_n(\Delta_n,\Delta_t) = \frac{\Gamma_n}{\delta_n}\left[m\left(1-\frac{\Delta_n}{\delta_n}\right)^{\alpha}\left(\frac{m}{\alpha}+\frac{\Delta_n}{\delta_n}\right)^{m-1} - \alpha\left(1-\frac{\Delta_n}{\delta_n}\right)^{\alpha-1}\left(\frac{m}{\alpha}+\frac{\Delta_n}{\delta_n}\right)^{m}\right] \times\left[\Gamma_t\left(1-\frac{|\Delta_t|}{\delta_t}\right)^{\beta}\left(\frac{n}{\beta}+\frac{|\Delta_t|}{\delta_t}\right)^{n} + \langle\phi_t-\phi_n\rangle\right]$$
$$T_t(\Delta_n,\Delta_t) = \frac{\Gamma_t}{\delta_t}\left[n\left(1-\frac{|\Delta_t|}{\delta_t}\right)^{\beta}\left(\frac{n}{\beta}+\frac{|\Delta_t|}{\delta_t}\right)^{n-1} - \beta\left(1-\frac{|\Delta_t|}{\delta_t}\right)^{\beta-1}\left(\frac{n}{\beta}+\frac{|\Delta_t|}{\delta_t}\right)^{n}\right] \times\left[\Gamma_n\left(1-\frac{\Delta_n}{\delta_n}\right)^{\alpha}\left(\frac{m}{\alpha}+\frac{\Delta_n}{\delta_n}\right)^{m} + \langle\phi_n-\phi_t\rangle\right]\frac{\Delta_t}{|\Delta_t|} \tag{8}$$

The shear tractions, T_{t1} and T_{t2}, are subsequently determined from (2). The normal, shear, and effective shear tractions are plotted in Fig. 3 for $\phi_t > \phi_n$, quasi-brittle behavior for mode I, and plateau-type behavior for modes II and III.

2.3. Implementation in FE frameworks

For details regarding the formulation of the material tangent stiffness matrix, **D,** and provisions for unloading/reloading and contact, refer to Appendix A. Of particular interest:

- The traction–separation relation for the 3D implementation is defined by ϕ_n, ϕ_t, λ_n, λ_t, σ_{max}, τ_{max}, α, and β, the same as the 2D implementation.
- Resistance to sliding in the two shearing directions is equal—T_{t1} and T_{t2} are not scaled to yield anisotropic sliding behavior, but could theoretically be altered to do so.
- The normal conjugate final crack opening width is determined by solving the nonlinear equation:

$$T_n(\Delta_n = 0, \Delta_t = \bar{\delta}_t) = 0 = \frac{\Gamma_n}{\delta_n}\left[m\left(\frac{m}{\alpha}\right)^{m-1} - \alpha\left(\frac{m}{\alpha}\right)^{m}\right]\left[\Gamma_t\left(1 - \frac{|\Delta_t|}{\delta_t}\right)^{\beta}\left(\frac{n}{\beta} + \frac{|\Delta_t|}{\delta_t}\right)^{n} + \langle\phi_t - \phi_n\rangle\right], \tag{10}$$

while the tangential conjugate final crack opening width follows in the same manner from:

$$T_t(\Delta_n = \bar{\delta}_n, \Delta_t = 0) = 0 = \frac{\Gamma_t}{\delta_t}\left[n\left(\frac{n}{\beta}\right)^{n-1} - \beta\left(\frac{n}{\beta}\right)^{n}\right]\left[\Gamma_n\left(1 - \frac{\Delta_n}{\delta_n}\right)^{\alpha}\left(\frac{m}{\alpha} + \frac{\Delta_n}{\delta_n}\right)^{m} + \langle\phi_n - \phi_t\rangle\right]. \tag{11}$$

- The PPR model is implemented in ABAQUS as an 8-noded UEL with four integration points in the natural coordinate system over the domain $-1 \leqslant \xi \geqslant 1$ and $-1 \leqslant \eta \geqslant 1$.

$$\begin{aligned} &\xi = -0.707 \quad \eta = -0.707 \\ &\xi = 0.707 \quad \eta = -0.707 \\ &\xi = 0.707 \quad \eta = 0.707 \\ &\xi = -0.707 \quad \eta = 0.707 \end{aligned}$$

The isoparametric formulation is given in Fig. 4, where **K** is the element stiffness matrix, **f** the internal force vector, **B** the strain–displacement matrix, and **|J|** the determinant of the Jacobian.

- The initial thickness of a cohesive element is simply the distance in the normal direction between nodes belonging to the same nodal pair. For zero-thickness cohesive elements, the two nodes forming a pair are initially collapsed upon one another. For cohesive elements with an initial thickness, this thickness is not included in the measure for Δ_n as cohesive normal separation is a relative measure.

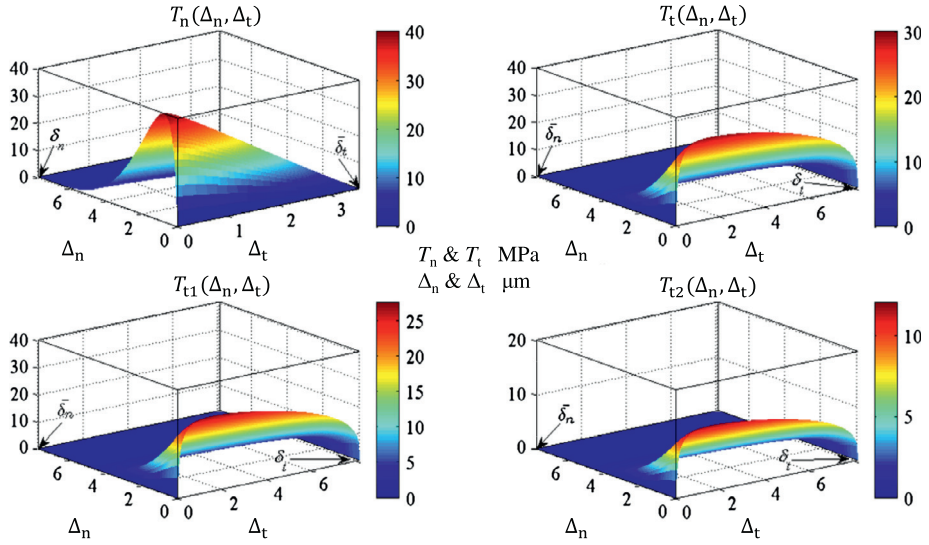

Fig. 3. Cohesive tractions with ϕ_n = 100 N/m, ϕ_t = 200 N/m, σ_{max} = 40 MPa, τ_{max} = 30 MPa, α = 5, β = 1.3, λ_n = 0.1, and λ_t = 0.2. It is assumed that $\Delta_{t2} = 0.4\Delta_t$, where $\Delta_{t1} = \sqrt{\Delta_t^2 - \Delta_{t2}^2}$.

$$
\begin{aligned}
N1 &= \frac{1}{4}(1-\varepsilon)(1-\eta)\\
N2 &= \frac{1}{4}(1+\varepsilon)(1-\eta)\\
N3 &= \frac{1}{4}(1+\varepsilon)(1+\eta)\\
N4 &= \frac{1}{4}(1-\varepsilon)(1+\eta)
\end{aligned}
\qquad (12)
$$

$$\mathbf{K} = \int_{-1}^{1}\int_{-1}^{1} \mathbf{B}^{T}\mathbf{D}\mathbf{B}|\mathbf{J}|\,d\xi\,d\eta \qquad (13)$$

$$\mathbf{f} = \int_{-1}^{1}\int_{-1}^{1} \mathbf{B}^{T}\mathbf{t}|\mathbf{J}|\,d\xi\,d\eta \qquad (14)$$

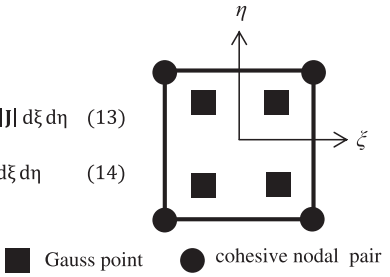

Fig. 4. Isoparamteric formulation of 8-noded cohesive elements.

- Finite Element All-Wheel Drive (FEAWD) is employed for HPC applications. FEAWD is an "in-house" high performance research finite element code developed at Cornell University. It is built on MPI, FemLib, PETSc [22–24], ParMETIS, and HDF5.

3. Application case studies

3.1. Mode I: T-peel specimen

Debonding is investigated in aluminum/epoxy T-peel joints. Mechanical tests performed by Alfano et al. [25] and Alfano [26] using the T-peel joint specimen, Fig. 5(a), investigated bond strengths for grit blasted specimens. The experiment is simulated here in both 2D (plane stress) and 3D using the PPR model.

The bulk material, AA6085-T6, was modeled with a Mises plasticity model. The yield stress and plastic modulus were 250 MPa and 525.8 MPa, respectively. It was assigned a linear elastic, isotropic material model with $E = 68$ GPa and $\nu = 0.33$. The epoxy, Loctite Hysol 9466, was modeled with the PPR and was represented by a single layer of cohesive elements with an initial thickness of 0.25 mm. A maximum acceptable cohesive zone length was determined from the plastic zone size estimates discussed in Rice [27]. Both 2D and 3D models were loaded in displacement-control. The 2D mesh was composed of 4-noded bilinear elements with reduced integration and hourglass control (CPS4R) and four-noded, quadrilateral PPR UELs. The 3D mesh was composed of 8-noded linear bricks with reduced integration and hourglass control (C3D8R) and eight-noded PPR UELs of length 0.450 mm.

A comparison of the experimental results and the numerical simulations is given in Fig. 5(b). It is apparent that the 2D and 3D simulations qualitatively reproduce the experimental data within the error bounds. For the 2D simulations, the curves in Fig. 5(b) do not exhibit the fluctuations in post-peak strength which the 3D simulations and experimental results reflect.

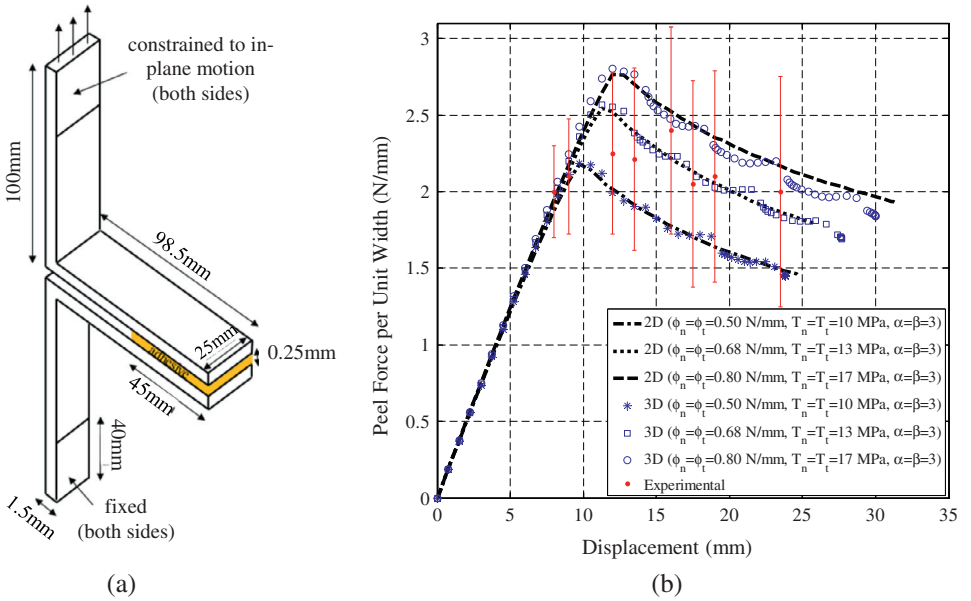

Fig. 5. T-peel joint specimen (a) and comparison between experimental data and numerical simulations (b).

Given that the adhesive is a ductile material, it would seem that relatively low shape parameters, α and β, would replicate more accurately experimental behavior; however, as Fig. 6 suggests, the 3D solution shows no sensitivity to softening behavior.

3.2. Modes I and II: mixed-mode bending (MMB) specimen

The MMB specimen is detailed in ASTM standard D 6671/D 6671M [28]. The MMB test [29], a combination of the double cantilever beam and end-notch flexure tests, was developed by Reeder and Crews and is used widely to investigate mixed-mode fracture in composites, Fig. 7.

Numerical simulations with the PPR model replicating the MMB test were conducted in 2D by Park et al. [21], and the numerical results were compared against the analytical solution given by Mi et al. [30]. The simulations are extended here to 3D using ABAQUS. A modified Riks method was employed to capture the negative stiffness of the load–displacement response. The zero-thickness cohesive elements were extended along the beam's midplane, just beyond the initial delamination. The mesh was composed of 0.398 mm-length 8-noded PPR UELs and 8-noded linear bricks with reduced integration and hourglass control (C3D8R). The specimen was assigned a linear elastic, isotropic material model with E = 122 GPa and ν = 0.25. Informed by Park et al. [21], the initial slope indicators λ_n and λ_t were assigned values 0.005 and 0.025, respectively,

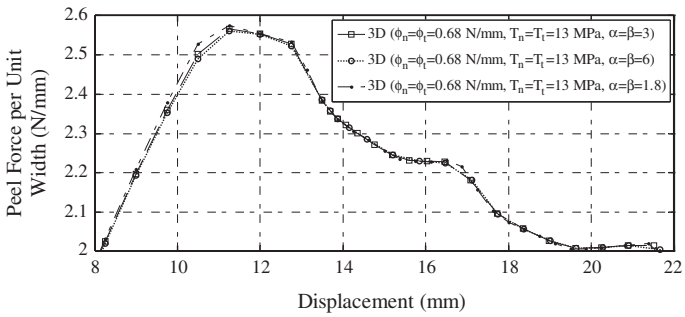

Fig. 6. Comparison of 3D numerical simulations with varying softening behaviors.

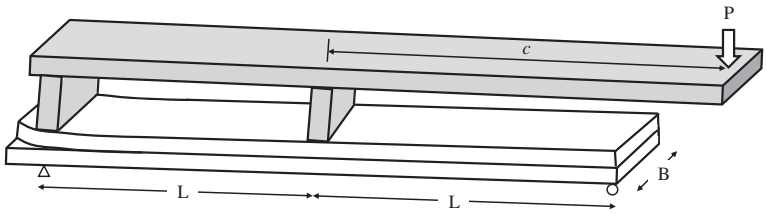

Fig. 7. MMB specimen. In the actual test, a load P is applied to a rigid lever (which is connected to the specimen) a distance c from the specimen's midspan. L = 51.0 mm and c = 60 mm for geometry modeled.

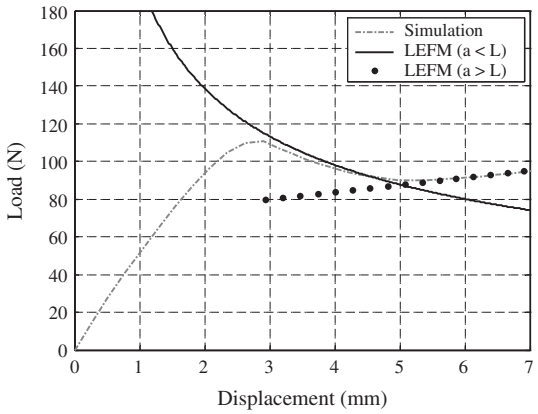

Fig. 8. Plot of load (P) vs. crack opening displacement measured below hinge connection. Analytical solution overlaid.

while the shape parameters α and β were both assigned a value of 3. Normal and tangential cohesive strengths, σ_{max} and τ_{max}, were both set to 10 MPa and the normal and tangential fracture energies, ϕ_n and ϕ_t, were 0.5 N/mm.

A comparison of the analytical solution and numerical simulation is given in Fig. 8. Notice that the simulation results converge to the analytical.

3.3. Modes II and III: edge crack torsion (ECT) specimen

The edge crack torsion (ECT) specimen is used to characterize mode III delamination fracture in laminated composites. Considering Ratcliffe's modified ECT specimen [31], Fig. 9, the rectangular specimen has an edge delamination at the midplane. Two pins impart load to the specimen in a symmetric fashion causing Mode III shear sliding at the midplane. Mode II develops at the edges of the specimen. Ratcliffe's modified ECT specimen is considered here for verification of the three-dimensional PPR model under mixed-mode loading.

The material is S2/8552, a glass-epoxy prepreg, with properties given in Table 1 [32]. The stacking sequence was $[90/0/(+45/-45)_7/(-45/+45)_7/0/90]_s$, with each ply modeled as a single, orthotropic layer. The specimen was modeled in ABAQUS with 8-noded linear bricks with reduced integration and hourglass control (C3D8R) and 8-noded PPR UELs ranging in length from 0.210 mm to 1.0 mm. The two crack surfaces were assigned frictionless tangential contact controls, and to prevent interpenetration, augmented Lagrangian contact controls were assigned. The specimen was loaded on the top surface via two node-based kinematic boundary conditions in the z-direction. Roller supports were positioned on the bottom, min-x, and max-y surfaces, per Fig. 9.

A visualization of the deformed configuration and a load–displacement plot with simulation and Ratcliffe's experimental results [31] are given in Figs. 10 and 11, respectively. Two initial crack lengths, 15.2 mm and 19.0 mm, were investigated. From a calibration study on the a = 19.0 mm configuration, each cohesive element at the midplane was assigned parameters ϕ_n = 1.5 N/mm, ϕ_t = 4.7 N/mm, $\sigma_{max} = \tau_{max}$ = 58 MPa, $\lambda_n = \lambda_t$ = 0.002, and $\alpha = \beta$ = 6. For the uncalibrated a = 15.2 mm configuration, the numerical simulation's peak load was approximately 4560 N at displacement 3.9 mm, 180 N higher than the experimental peak at displacement 3.6 mm. It is apparent that the PPR-based simulations can reproduce observed Mode II/III behavior within a reasonable tolerance.

3.4. Dynamic analysis: Battelle Drop-Weight Tear Test

The Battelle Drop-Weight Tear (BDWT) test is used commonly in the steel pipeline industry to determine transition temperature based on evaluated fracture surface appearance. Recent investigations in Igi et al. [33] and Nonn and Kalwa [34] are focused on the study of this test to determine the crack propagation characteristics of long-running ductile cracks,

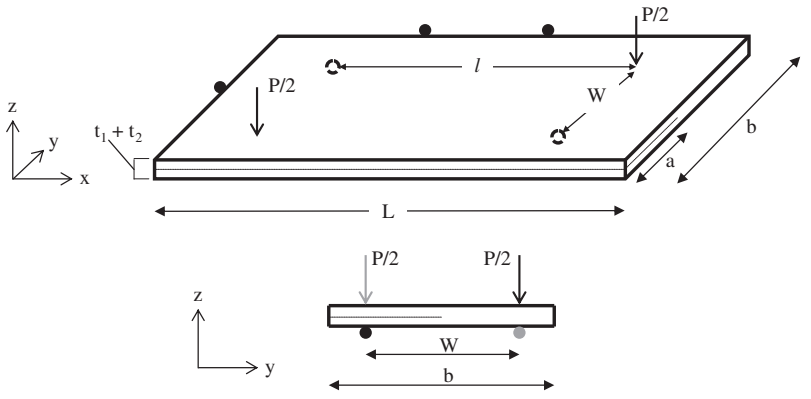

Fig. 9. Modified ECT specimen. L = 108 mm, l = 76 mm, b = 38 mm, W = 32 mm, $t_1 = t_2$ = 3.75 mm, a = variable. The circles represent roller supports.

Table 1
S2/8552 material properties.

Property	Value
E_{11}	47.71 GPa
E_{22}, E_{33}	12.27 GPa
ν_{12}, ν_{13}	0.278
ν_{23}	0.403
G_{12}, G_{13}	4.83 GPa
G_{23}	4.48 GPa

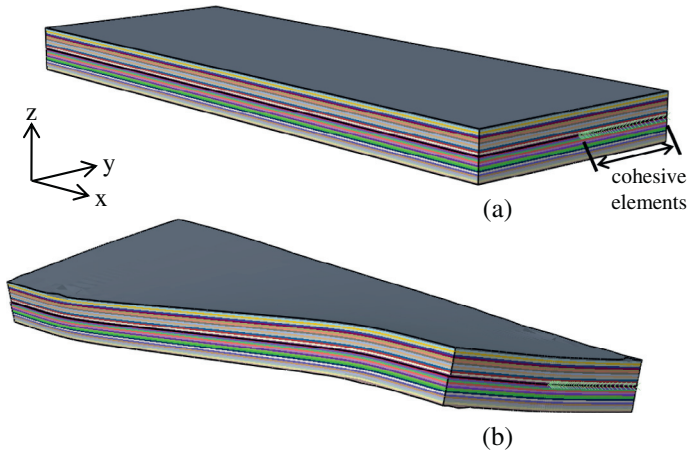

Fig. 10. Undeformed (a) and deformed (b) configurations of ECT numerical model. Colors denote plies. (For interpretation of the references to color in this figure legend, the reader is referred to the web version of this article.)

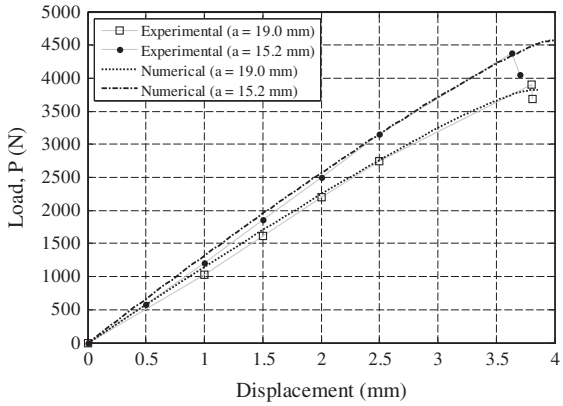

Fig. 11. Numerical and experimental load–displacement curves for ECT test.

specifically the crack arrest capabilities of the underlying material. Associated standards are given in the following references [35–37]. A schematic of the apparatus showing hammer, supports, and test specimen is given in Fig. 12(a). This test was conducted with drop energy of 105 kJ resulting from a hammer weight of 2.8 tonnes and falling height of 3.8 m. The test specimen was a rectangular bar with dimensions of 76 mm height, 305 mm length, and a thickness corresponding to the thickness of linepipe, here 18.4 mm. The full thickness specimen extracted circumferentially from the pipe contained a 5 mm pressed notch to increase the probability of cleavage fracture initiation at the root of the notch. When the specimen was impacted in three-point bending, a crack nucleated at the root of the pressed notch and propagated upwards towards the hammer. The test was conducted at room temperature and instrumented to register force vs. time curves, which allow for the determination of specific crack initiation and propagation energies. In addition, shear area fractions were evaluated from the appearance of the fracture surface without considering a length equal to the pipe thickness at each end. This is due to the fact that the material below the notch and at the back end of the specimen experiences work hardening during the indentation of the notch and by the impact of the hammer, respectively.

The BDWT experimental results presented in Nonn and Kalwa [34] are used here to gauge the suitably of the PPR in describing the fracture behavior in X100 steel under dynamic loading. The analysis was dynamic with an implicit integration solution scheme. The finite element analyses were performed using ABAQUS. By means of symmetry, only a fourth of the specimen was modeled. The support and hammer were modeled as analytical rigid bodies, the specimen with 8-noded linear bricks with reduced integration and hourglass control (C3D8R), and the crack path with 0.414 mm-length 8-noded PPR UELs. The X100 steel was modeled by a rate-sensitive Mises plasticity model with the flow curve given in Fig. 12(b) and elastic properties $E = 210$ GPa and $\nu = 0.30$. The flow curve was formulated from experimental data and is valid until the onset of uniform elongation; thereafter, the extension of the curve is represented by the power law function ($\sigma = K\varepsilon_p^n$). Strength coefficient $K = 897.8$ MPa and strain hardening exponent $n = 0.0321$ were adjusted to the experimental stress–strain data. The strain rate dependence of the material was accounted for in the plasticity model by defining the yield strength values as a function of different strain rate levels.

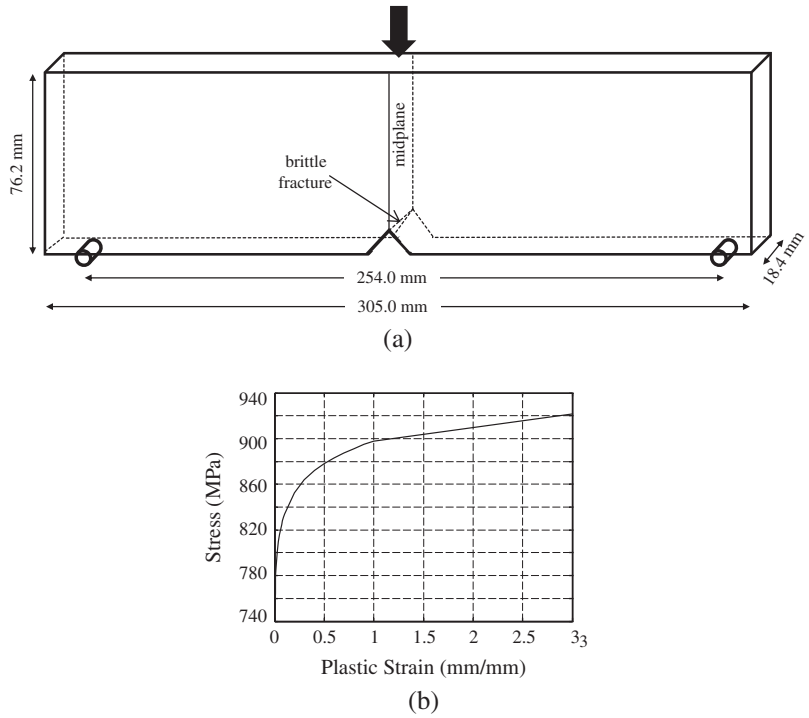

Fig. 12. Battelle Drop-Weight Tear test (BDWT) test specimen and simplified apparatus (a) and flow curve for rate sensitive Mises plasticity model (b).

The PPR model was employed to capture experimentally observed behavior. The parameters were estimated based on the literature recommendations in Negre et al. [38], Roy and Dodds [39], and Scheider et al. [40] (e.g. cohesive strength should lie in the range 2.0–3.0 $\times$ yield stress, $\sim$700 MPa, and the fracture energy corresponds approximately to the J-integral value at initiation, 240 N/mm). Cohesive elements along the entire length of the midplane were assigned $\lambda_n = \lambda_t = 0.002$. Three sets of PPR parameters were considered in the present study. A visualization of the deformed configuration, PPR parameters, and a load–time plot with simulation and experimental results are given in Fig. 13.

Two of the simulations employed PPR parameters indicative of X100, but considered different softening behaviors. The third used a substantially smaller cohesive strength and higher fracture energy to better replicate post-peak behavior, particularly for time >4 ms. Here, cohesive strength dictates the maximum load-bearing capacity of the beam while the fracture energy dictates to what extent this load can be carried—the higher the fracture energy, the longer the beam can sustain the hammer's impact.

Ductile softening behavior (i.e. plateau-type) most accurately captured peak, but did a relatively poor job capturing decay. Brittle softening, on the other hand, caused more rapid decay behavior while only underestimating the experimental peak by approximately 5% (0.5 ms before the experimental peak). Physically realistic PPR parameters (ϕ = 240 N/mm, σ = 2000 MPa, $\alpha = \beta = 6$) for X100 roughly replicated decay behavior, but underpredicted the decay for time >4 ms. For the simulation with a relatively high fracture energy, the decay for time >4 ms was more accurately characterized.

3.5. Intergranular fracture

Intergranular fracture, commonly referred to as grain boundary decohesion, is a highly complex fracture phenomenon governed by many microstructural characteristics including grain size, shape, and orientation. One of the first studies investigating intergranular fracture was conducted in two-dimensions by Raj and Ashby [41]. With the advent of microstructure generation toolsets, robust surface and volumetric meshing routines, massively parallelized finite element drivers and accompanying HPC solutions, and the PPR model, it is now possible to model three-dimensional grain boundary decohesion and avoid numerical difficulties such as locking.

A polycrystal discretized along the grain boundaries with cohesive elements is an ideal medium by which to explain locking. Here locking is defined as a numerical phenomenon marked by a nonlinear solver's inability to reach a converged solution because an insufficient number of load paths exist to accommodate additional deformation. In a polycrystal, if a soft grain is pinned between stiffer grains, the cohesive elements surrounding the soft grain allow additional deformation insofar that they do not completely fail. If too many cohesive elements fail, the soft grain no longer has a release by which to unload accumulated deformation. Consequently, the model "locks" in place as the nonlinear solver is unable to reach a converged solution.

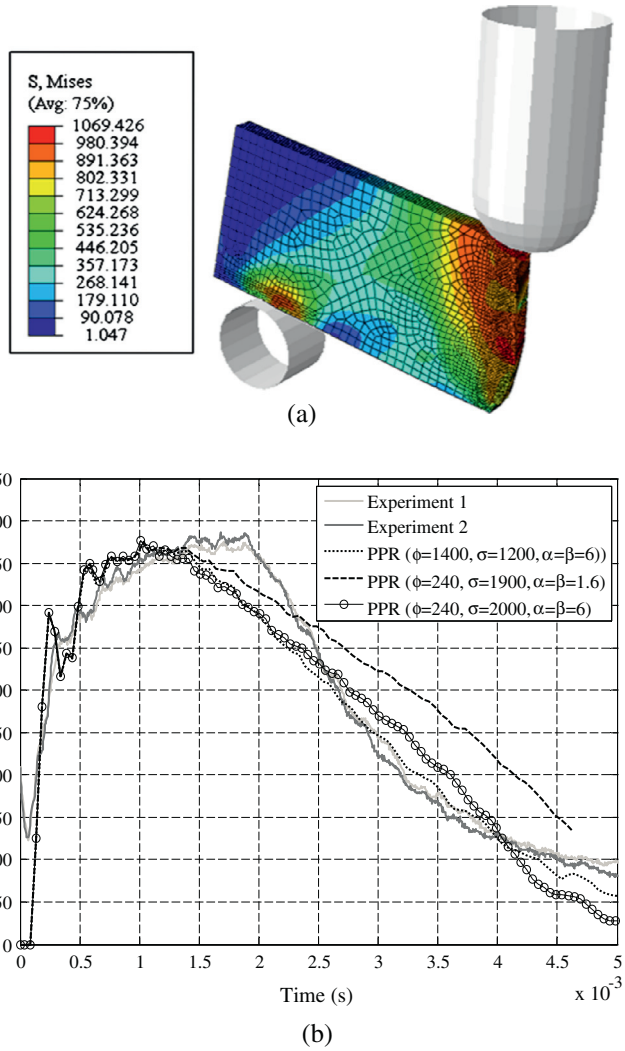

Fig. 13. BDWT test deformed configuration at time = 2.8 ms with Von Mises stress (MPa) overlaid (a) and comparison of the specimen's load bearing capacity versus time, experimental and numerical (b).

Iesulauro [6] modeled grain boundary decohesion in synthetically generated microstructures with a three-dimensional adaptation of the Tvergaard and Hutchinson [7] coupled cohesive zone model. The model couples the normal and tangential tractions and displacements into coupled measures. Mode-mixity is considered through the interaction formula:

$$D = \sqrt{\left(\frac{\Delta_n}{\delta_n}\right)^2 + \left(\frac{\Delta_t}{\delta_t}\right)^2}, \tag{15}$$

where the influence of normal and shear is proportional. When $D = 1$, the cohesive surface loses all ability to transmit traction.

Consider the scenario where a grain boundary is loaded normally so that it no longer has the capacity to transmit traction normally. If modeled with a coupled CZM, the interface has no capacity to transmit traction in either mode, a physically realistic behavior. If modeled with an uncoupled CZM without regard for energetically consistent boundary conditions, the interface will continue to transmit traction tangentially and yield physically unrealistic behavior. If modeled with the PPR, the interface will fail normally and still be able to transmit tangential tractions, as long as $\Delta_n < \bar{\delta}_n$. The PPR is preferred for this application not only because it replicates physically realistic behavior, but also, in the presence of mode-I, II, or III failure, preserves the cohesive interactions of the un-failed modes according to the final crack opening and conjugate final crack opening widths.

To demonstrate the PPR model's ability to model intergranular fracture, a synthetic polycrystal generated with a Voronoi tessellation technique was considered. The microstructure was volumetrically meshed with tetrahedra, cohesive elements

were inserted along the grain boundaries, and the model was loaded statically in simple tension with a 3% applied strain, Fig. 14. One analysis was performed with the PPR model describing the constitutive response of the grain boundaries; a second analysis was performed with the Tvergaard and Hutchinson coupled CZM.

The cohesive parameters used in the analyses are given in Tables 2 and 3. Note that the parameters were chosen to yield nearly identical cohesive behavior. For example, cohesive strengths, final crack opening widths, and softening behavior were matched, rendering discrepancies in numerical metrics like solver convergence solely the product of the coupled/uncoupled nature of the models. The bulk material was assigned linear elastic, isotropic behavior with $E = 75$ GPa and $\nu = 0.33$.

FEAWD was used to formulate and solve the nonlinear system, employing a trust region nonlinear solver, a conjugate gradient Krylov subspace method, and a Jacobi preconditioner as implemented in PETSc. The default linear and nonlinear solver tolerances were used. Converged function norms for the analyses are given in Fig. 15. Here, convergence is reached once the l^2-norm of the residual is less than or equal to the product of the l^2-norm of the residual evaluated at the initial guess and a

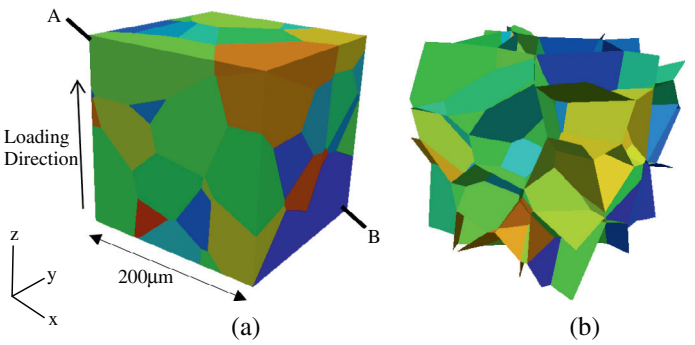

Fig. 14. Cubic polycrystal model (a) and corresponding cohesive grain boundary surfaces (b).

Table 2
PPR model parameters.

σ_{max}, τ_{max}	ϕ_n, ϕ_t	λ_n, λ_t	α, β
450 MPa	1136 N/mm	0.005	2

Table 3
Coupled CZM parameters.

$T_{max\ coupled}$	k_o	δ_n, δ_t
450 MPa	$50 * T_{max\ coupled}$	0.005 mm

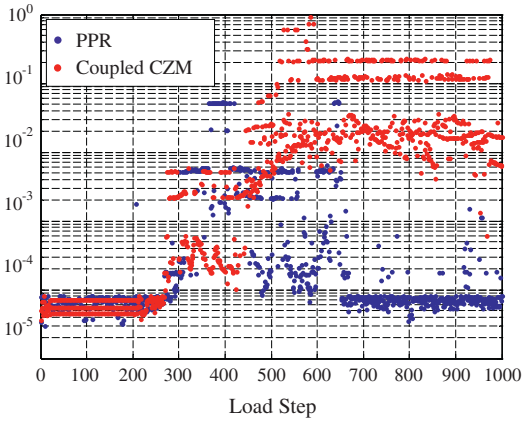

Fig. 15. Nonlinear function norms for polycrystal analysis.

user-specified relative tolerance (1e−4 in this study). It is apparent that once an appreciable amount of cohesive softening was initiated in the polycrystal, the nonlinear solver in the coupled CZM analysis struggled to converge to pre-softening levels, raising doubts about the accuracy of the resulting output. The nonlinear solver in the PPR analysis, on the other hand, had some difficulty reaching pre-softening levels of convergence for the intermediate load steps; however, unlike the coupled analysis, the solver fully recovered for the final 300 load steps.

Locking can be blamed for the convergence trend of the coupled CZM analysis. Referring to Fig. 16, a plot of stress in the loading direction at 2.4% strain across line A-B in Fig. 14(a), it is apparent that the models converged to different answers. While both models developed a through crack at the same location, the stresses in Fig. 16 indicate an abnormality in the

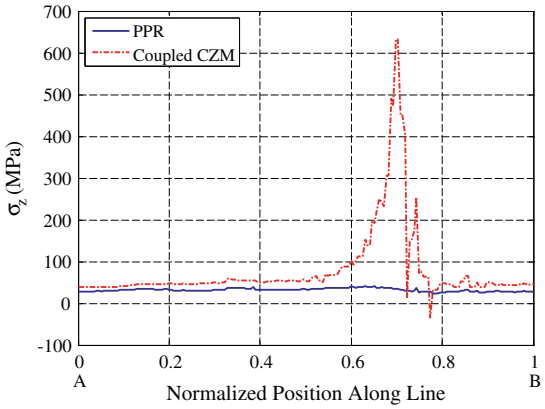

Fig. 16. Plot of σ_z along line A-B shown in Fig. 15(a) at 2.4% strain.

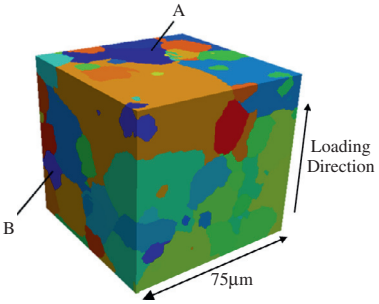

(a)

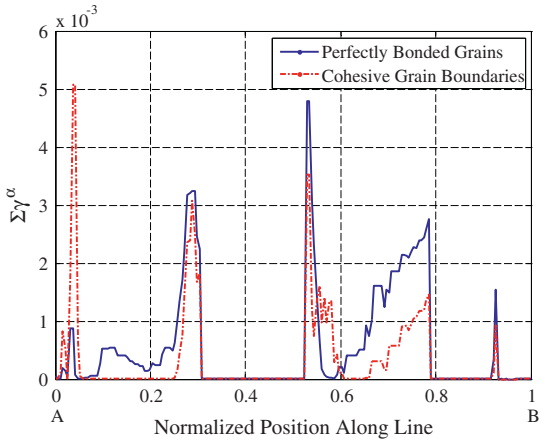

(b)

Fig. 17. DREAM.3D-generated cubic polycrystal (a) and sum of slips on FCC octahedral and cubical slip systems throughout polycrystal at 0.30% strain, with and without PPR CZM on grain boundaries (b).

center of the coupled model. It is apparent that the PPR model has nearly completely unloaded; however, the coupled model has obviously retained a significant capacity to resist complete decohesion. Given the unrealistic nature of this result, particularly a small segment of a grain boundary being able to resist complete decohesion, and the nonlinear solver's poor performance discussed previously, it is apparent that the coupled CZM model's solution is unrealistic while the PPR model is physically acceptable.

The PPR model's application in a polycrystalline finite element analysis is discussed here. DREAM.3D [42,43] was used to create a statistically representative 240-grain microstructure of a nickel-based superalloy with an annealed twin in the center; the geometry was volume meshed, with cohesive elements along the grain boundaries, loaded in simple tension, and analyzed in FEAWD, Fig. 17(a). A grain-size-sensitive crystal plasticity model was employed to model bulk behavior while the PPR model accounted for grain boundary decohesion. A model with perfectly bonded grains and another with PPR cohesive grain boundaries were considered.

The mesh with cohesive grain boundaries had 12.6-million degrees-of-freedom (DOFs) and 272,636 quadratic, triangular cohesive elements. The simulation ran on 512 processors on the Texas Advanced Computing Center's Sun Constellation Linux cluster Ranger for approximately twelve hours before slip began to accumulate on the slip systems. The sum of the accumulated irreversible slip on the six cubical and twelve octahedral slips systems, $\sum_{\alpha=1}^{18}\gamma^{\alpha}$, was considered throughout both polycrystals, mapped to a line extending from A to B in Fig. 17(a) as shown in Fig. 17(b). Grain boundary decohesion altered the slip state in the microstructure, in some grains facilitating slip while in others impeding it.

Intergranular fracture is a complex microstructural deformation mechanism, and the investigations presented herein are included simply to motivate further study and establish the PPR model as an adequate means to address this phenomenon in a HPC FE framework. Obviously, to model this mechanism accurately, cohesive parameters would need to be calibrated, and there is no guarantee that a single set of parameters would be appropriate for every grain boundary in the microstructure. For example, special consideration would need to be paid to triple junctions and twin boundaries.

4. Conclusions and extensions

This paper has detailed the PPR model's extension to three-dimensions and demonstrated its efficacy in modeling mixed-mode fracture in single-core and HPC applications across a variety of applications. A description of the PPR model in relation to the prevailing cohesive zone modeling methodologies, its formulation in three-dimensions, and its implementation in a three-dimensional finite element framework were given. Appendix A contains a formulation of the material tangent stiffness matrix and provisions for unloading/reloading and contact.

The T-peel joint (mode I), MMB (modes I and II), and ECT (modes II and III) specimens were modeled to verify the three-dimensional PPR implementation. The T-peel PPR simulations yielded experimentally-consistent Mode I behavior. The MMB PPR simulation reproduced accurately the analytically-predicted results. The ECT simulations, with both Mode II and III components, yielded experimentally-consistent load–displacement data for different crack lengths. The Battelle Drop Weight Tear test was modeled to demonstrate the PPR model's capability for dynamic loading and gauge its ability to model the high rate of crack propagation inherent to the experiment. Here, the PPR model was shown to capture adequately experimental load-bearing behavior. Finally, the case of intergranular fracture was considered to demonstrate the PPR model's performance under severe mode-mixity in a HPC environment. It was shown that the PPR model outperforms a coupled CZM in modeling intergranular fracture, not only because it is energetically consistent, but also because it does not present the nonlinear solver a computationally intractable problem to solve. The PPR model, therefore, could be extended to many applications where the crack path is not known *a priori* and the loading is such that a high degree of mode-mixity exists in the continuum.

Such extensions could use the PPR model (as described in this paper) as the basic platform in which additional physics could be inserted. These extensions include anisotropic sliding behavior (as pointed out in Section 2.3), rate dependency in the traction–separation relationship, healing effect (relevant for asphalt and other polymer-based composites), and functionally graded cohesive behavior to account for interphase changes (in this case the cohesive properties are functions and not constants anymore). Some of these issues are currently being pursued by the authors.

Acknowledgements

This research was funded by the Air Force Office of Scientific Research under grant number FA9550-10-1-0213, supervised by Dr. David Stargel. This work used the Extreme Science and Engineering Discovery Environment (XSEDE), which is supported by National Science Foundation (NSF) grant number OCI-1053575. In addition, we also thank NSF through grant CMMI-1321661. Support from the Donald B. and Elizabeth M. Willett endowment at the University of Illinois at Urbana-Champaign (UIUC) is gratefully acknowledged, as is support from the Ross-Tetelman Fellowship at Cornell University. The authors would also like to acknowledge Dr. Gerd Heber of the HDF Group for assistance with FEAWD and Dr. Joe Tucker of Carnegie Mellon University's Department of Materials Science and Engineering for generating the 240-grain microstructure considered in the intergranular fracture case study. Any opinion, finding, conclusions or recommendations expressed here are those of the authors and do not necessarily reflect the views of the sponsors.

Appendix A. Material tangent matrix

A.1. Formulation

The material tangent stiffness matrix **D** is defined as follows:

$$D_{ij} = \frac{\partial T_i}{\partial \Delta_j} \tag{A.1}$$

$$\mathbf{D} = \begin{bmatrix} \frac{\partial T_{t1}(\Delta_n,\Delta_{t1},\Delta_{t2})}{\partial \Delta_{t1}} & \frac{\partial T_{t1}(\Delta_n,\Delta_{t1},\Delta_{t2})}{\partial \Delta_{t2}} & \frac{\partial T_{t1}(\Delta_n,\Delta_{t1},\Delta_{t2})}{\partial \Delta_n} \\ \frac{\partial T_{t2}(\Delta_n,\Delta_{t1},\Delta_{t2})}{\partial \Delta_{t1}} & \frac{\partial T_{t2}(\Delta_n,\Delta_{t1},\Delta_{t2})}{\partial \Delta_{t2}} & \frac{\partial T_{t2}(\Delta_n,\Delta_{t1},\Delta_{t2})}{\partial \Delta_n} \\ \frac{\partial T_n(\Delta_n,\Delta_t)}{\partial \Delta_{t1}} & \frac{\partial T_n(\Delta_n,\Delta_t)}{\partial \Delta_{t2}} & \frac{\partial T_n(\Delta_n,\Delta_t)}{\partial \Delta_n} \end{bmatrix} \tag{A.2}$$

for $i = 1, 2$

$$\frac{\partial T_{ti}}{\partial \Delta_n} = \frac{\partial T_n}{\partial \Delta_{ti}} = \frac{\Gamma_t \Gamma_n \Delta_{ti}}{\delta_t \delta_n \Delta_t}\left[n\left(1-\frac{\Delta_t}{\delta_t}\right)^{\beta}\left(\frac{n}{\beta}+\frac{\Delta_t}{\delta_t}\right)^{n-1} - \beta\left(1-\frac{\Delta_t}{\delta_t}\right)^{\beta-1}\left(\frac{n}{\beta}+\frac{\Delta_t}{\delta_t}\right)^{n}\right]\left(-\frac{\alpha\left(1-\frac{\Delta_n}{\delta_n}\right)^{\alpha}\left(\frac{m}{\alpha}+\frac{\Delta_n}{\delta_n}\right)^{m}}{1-\frac{\Delta_n}{\delta_n}} + \frac{m\left(1-\frac{\Delta_n}{\delta_n}\right)^{\alpha}\left(\frac{m}{\alpha}+\frac{\Delta_n}{\delta_n}\right)^{m}}{\left(\frac{m}{\alpha}-\frac{\Delta_n}{\delta_n}\right)}\right) \tag{A.3}$$

for $i = 1, 2$

$$\begin{aligned}\frac{\partial T_{ti}}{\partial \Delta_{ti}} = {} & \left[\Gamma_n\left(1-\frac{\Delta_n}{\delta_n}\right)^{\alpha}\left(\frac{m}{\alpha}+\frac{\Delta_n}{\delta_n}\right)^{m} + \langle \phi_n - \phi_t \rangle\right] \\ & \times \left(\frac{\Delta_{ti}^2 \Gamma_t}{\delta_t^2 \Delta_t^2}\left[-\frac{n\beta\left(1-\frac{\Delta_t}{\delta_t}\right)^{\beta}\left(\frac{n}{\beta}+\frac{\Delta_t}{\delta_t}\right)^{n-1}}{1-\frac{\Delta_t}{\delta_t}} + \frac{n(n-1)\left(1-\frac{\Delta_t}{\delta_t}\right)^{\beta}\left(\frac{n}{\beta}+\frac{\Delta_t}{\delta_t}\right)^{n-1}}{\frac{n}{\beta}+\frac{\Delta_t}{\delta_t}} + \frac{\beta(\beta-1)\left(1-\frac{\Delta_t}{\delta_t}\right)^{\beta-1}\left(\frac{n}{\beta}+\frac{\Delta_t}{\delta_t}\right)^{n}}{1-\frac{\Delta_t}{\delta_t}} - \frac{\beta n\left(1-\frac{\Delta_t}{\delta_t}\right)^{\beta-1}\left(\frac{n}{\beta}+\frac{\Delta_t}{\delta_t}\right)^{n}}{\frac{n}{\beta}+\frac{\Delta_t}{\delta_t}}\right] \right. \\ & \left. + \left(n\left(1-\frac{\Delta_t}{\delta_t}\right)^{\beta}\left(\frac{n}{\beta}+\frac{\Delta_t}{\delta_t}\right)^{n-1} - \beta\left(1-\frac{\Delta_t}{\delta_t}\right)^{\beta-1}\left(\frac{n}{\beta}+\frac{\Delta_t}{\delta_t}\right)^{n}\right)\frac{\Gamma_t}{\delta_t}\left[\frac{1}{\Delta_t} - \frac{\Delta_{ti}}{\left(\Delta_{t1}^2+\Delta_{t2}^2\right)^{3/2}}\right]\right)\end{aligned} \tag{A.4}$$

$$\begin{aligned}\frac{\partial T_{t1}}{\partial \Delta_{t2}} = \frac{\partial T_{t2}}{\partial \Delta_{t1}} = {} & \Gamma_t \Delta_{t1}\Delta_{t2}\beta(n+\beta)\left[\Gamma_n\left(1-\frac{\Delta_n}{\delta_n}\right)^{\alpha}\left(\frac{m}{\alpha}+\frac{\Delta_n}{\delta_n}\right)^{m} + \phi_n - \phi_t\right] \\ & \times \left[\frac{\beta\left(1-\frac{\Delta_t}{\delta_t}\right)^{\beta}\left(\frac{n}{\beta}-\frac{\Delta_t}{\delta_t}\right)^{n}}{(\delta_t-\Delta_t)^2(n\delta_t+\beta\Delta_t)\Delta_t} - \frac{\beta n\left(1-\frac{\Delta_t}{\delta_t}\right)^{\beta}\left(\frac{n}{\beta}-\frac{\Delta_t}{\delta_t}\right)^{n}}{(\delta_t-\Delta_t)(n\delta_t+\beta\Delta_t)^2\Delta_t} + \frac{\beta\left(1-\frac{\Delta_t}{\delta_t}\right)^{\beta}\left(\frac{n}{\beta}-\frac{\Delta_t}{\delta_t}\right)^{n}}{(\delta_t-\Delta_t)(n\delta_t+\beta\Delta_t)^2\Delta_t} - \frac{\left(1-\frac{\Delta_t}{\delta_t}\right)^{\beta}\left(\frac{n}{\beta}-\frac{\Delta_t}{\delta_t}\right)^{n}}{(\delta_t-\Delta_t)^2(n\delta_t+\beta\Delta_t)\Delta_t}\right]\end{aligned} \tag{A.5}$$

$$\begin{aligned}\frac{\partial T_n}{\partial \Delta_n} = {} & \frac{\Gamma_n}{\delta_n}\left[\Gamma_t\left(1-\frac{\Delta_t}{\delta_t}\right)^{\beta}\left(\frac{n}{\beta}+\frac{\Delta_t}{\delta_t}\right)^{n} - \phi_t - \phi_n\right] \\ & \times \left[-\frac{m(1-\frac{\Delta_n}{\delta_n})^{\alpha}\alpha\left(\frac{m}{\alpha}+\frac{\Delta_n}{\delta_n}\right)^{m-1}}{1-\frac{\Delta_n}{\delta_n}} + \frac{m\left(1-\frac{\Delta_n}{\delta_n}\right)^{\alpha}\left(\frac{m}{\alpha}+\frac{\Delta_n}{\delta_n}\right)^{m-1}(m-1)}{\frac{m}{\alpha}+\frac{\Delta_n}{\delta_n}} + \frac{\alpha(1-\frac{\Delta_n}{\delta_n})^{\alpha-1}(\alpha-1)\left(\frac{m}{\alpha}+\frac{\Delta_n}{\delta_n}\right)^{m}}{1-\frac{\Delta_n}{\delta_n}} - \frac{\alpha\left(1-\frac{\Delta_n}{\delta_n}\right)^{\alpha-1}\left(\frac{m}{\alpha}+\frac{\Delta_n}{\delta_n}\right)^{m}m}{\frac{m}{\alpha}+\frac{\Delta_n}{\delta_n}}\right]\end{aligned} \tag{A.6}$$

A.2. Unloading/reloading

Define Δ_n^{max} and Δ_t^{max} to be the maximum normal and tangential separations, respectively, reached during loading/unloading. If $\Delta_n = \Delta_n^{max}$ and $\Delta_t = \Delta_t^{max}$, meaning that both the normal and shear are in the loading phase, the material tangent stiffness matrix is given by Eq. (A.2).

If $\Delta_t < \Delta_t^{max}$ and $\Delta_t = \Delta_t^{max}$, meaning that the normal is in the unload/reload phase and shear is loading, the matrix is given by:

$$\mathbf{D} = \begin{bmatrix} \frac{\partial T_{t1}(\Delta_n^{max},\Delta_t,|\Delta_{t1}|)}{\partial \Delta_{t1}} & \frac{\partial T_{t1}(\Delta_n^{max},\Delta_t,|\Delta_{t1}|)}{\partial \Delta_{t2}} & \frac{\partial T_{t1}(\Delta_n^{max},\Delta_t,|\Delta_{t1}|)}{\partial \Delta_n} \\ \frac{\partial T_{t2}(\Delta_n^{max},\Delta_t,|\Delta_{t2}|)}{\partial \Delta_{t1}} & \frac{\partial T_{t2}(\Delta_n^{max},\Delta_t,|\Delta_{t2}|)}{\partial \Delta_{t2}} & \frac{\partial T_{t2}(\Delta_n^{max},\Delta_t,|\Delta_{t2}|)}{\partial \Delta_n} \\ \frac{\partial T_n(\Delta_n^{max},\Delta_t)}{\partial \Delta_{t1}}\frac{\Delta_n}{\Delta_n^{max}} & \frac{\partial T_n(\Delta_n^{max},\Delta_t)}{\partial \Delta_{t2}}\frac{\Delta_n}{\Delta_n^{max}} & \frac{T_n(\Delta_n^{max},\Delta_t)}{\Delta_n^{max}} \end{bmatrix} \tag{A.7}$$

If $\Delta_n = \Delta_n^{max}$ and $\Delta_t < \Delta_t^{max}$, meaning that the normal is loading and the shear is in the unload/reload phase, the matrix is given by:

$$\mathbf{D} = \begin{bmatrix} \frac{T_t(\Delta_n,\Delta_t^{max})}{\Delta_t^{max}} & 0 & \frac{\partial T_t(\Delta_n,\Delta_t^{max})}{\partial \Delta_n}\frac{|\Delta_{t1}|}{\Delta_t^{max}} \\ 0 & \frac{T_t(\Delta_n,\Delta_t^{max})}{\Delta_t^{max}} & \frac{\partial T_t(\Delta_n,\Delta_t^{max})}{\partial \Delta_n}\frac{|\Delta_{t2}|}{\Delta_t^{max}} \\ \frac{\partial T_n(\Delta_n,\Delta_t)}{\partial \Delta_{t1}} & \frac{\partial T_n(\Delta_n,\Delta_t)}{\partial \Delta_{t2}} & \frac{\partial T_n(\Delta_n,\Delta_t)}{\partial \Delta_n} \end{bmatrix} \tag{A.8}$$

Finally, if $\Delta_n < \Delta_n^{max}$ and $\Delta_t < \Delta_t^{max}$, meaning that the normal and shear are unloading/reloading, the matrix is given by:

$$\mathbf{D} = \begin{bmatrix} \frac{T_t(\Delta_n,\Delta_t^{max})}{\Delta_t^{max}} & 0 & \frac{\partial T_t(\Delta_n,\Delta_t^{max})}{\partial \Delta_n}\frac{|\Delta_{t1}|}{\Delta_t^{max}} \\ 0 & \frac{T_t(\Delta_n,\Delta_t^{max})}{\Delta_t^{max}} & \frac{\partial T_t(\Delta_n,\Delta_t^{max})}{\partial \Delta_n}\frac{|\Delta_{t2}|}{\Delta_t^{max}} \\ \frac{\partial T_n(\Delta_n^{max},\Delta_t)}{\partial \Delta_{t1}}\frac{\Delta_n}{\Delta_n^{max}} & \frac{\partial T_n(\Delta_n^{max},\Delta_t)}{\partial \Delta_{t2}}\frac{\Delta_n}{\Delta_n^{max}} & \frac{T_n(\Delta_n^{max},\Delta_t)}{\Delta_n^{max}} \end{bmatrix} \tag{A.9}$$

A.3. Contact

Material self-penetration is prevented through a penalty method. When $\Delta_n < 0$, the normal traction is given by:

$$T_n(\Delta_n < 0, \Delta_{t1}, \Delta_{t2}) = \Delta_n \left\{ \frac{\Gamma_n \alpha}{\delta_n^2} \left[-\left(\frac{m}{\alpha}\right)^{m-1} - \left(\frac{m}{\alpha}\right)^m \right] \left[\Gamma_t \left(\frac{n}{\beta}\right)^n + \phi_t - \phi_n \right] \right\}, \tag{A.10}$$

where the expression in braces, the penalty stiffness, is assigned to the D_{nn} entry of the material tangent stiffness matrix. The matrix is given by:

$$\mathbf{D} = \begin{bmatrix} \frac{\partial T_{t1}(0,\Delta_t,|\Delta_{t1}|)}{\partial \Delta_{t1}} & \frac{\partial T_{t1}(0,\Delta_t,|\Delta_{t1}|)}{\partial \Delta_{t2}} & 0 \\ \frac{\partial T_{t2}(0,\Delta_t,|\Delta_{t2}|)}{\partial \Delta_{t1}} & \frac{\partial T_{t2}(0,\Delta_t,|\Delta_{t2}|)}{\partial \Delta_{t2}} & 0 \\ 0 & 0 & \frac{\Gamma_n \alpha}{\delta_n^2}\left[-\left(\frac{m}{\alpha}\right)^{m-1} - \left(\frac{m}{\alpha}\right)^m \right] \left[\Gamma_t \left(\frac{n}{\beta}\right)^n + \phi_t - \phi_n \right] \end{bmatrix} \tag{A.11}$$

References

[1] Dugdale D. Yielding of steel sheets containing slits. J Mech Phys Solids 1960;8:100–4.
[2] Barenblatt GI. The mathematical theory of equilibrium cracks in brittle fracture. Adv Appl Mech 1962;7:55–129.
[3] Hillerborg A, Modeer M, Petersson P. Analysis of crack formation and crack growth in concrete by means of fracture mechanics and finite elements. Cem Concr Res 1976;6:773–81.
[4] Boone TJ, Wawrzynek PA, Ingraffea AR. Simulation of the fracture processes in rock with application to hydrofracturing. Int J Rock Mech Min Sci 1986;23:255–65.
[5] Needleman A. A continuum model for void nucleation by inclusion debonding. J Appl Mech-Trans ASME 1987;54:525–31.
[6] Iesulauro E. Decohesion of grain boundaries in statistical representations of aluminum polycrystals. Ph.D. Dissertation. Cornell University, Ithaca, NY; 2006.
[7] Tvergaard V, Hutchinson JW. The relation between crack growth resistance and fracture process parameters in elastic–plastic solids. J Mech Phys Solids 1992;40:1377–97.
[8] Scheider I, Brocks W. Simulation of cup-cone fracture using the cohesive model. Engng Fract Mech 2003;70:1943–61.
[9] Ingraffea AR, Gerstle WH, Gergely P, Saouma V. Fracture mechanics of bond in reinforced concrete. J Struct Engng 1984;110:871–90.
[10] Elices M, Guinea GV, Gomez J, Planas J. The cohesive zone model: advantages, limitations and challenges. Engng Fract Mech 2002;69:137–63.
[11] Park K, Paulino GH, Roesler J. Cohesive fracture model for functionally graded fiber reinforced concrete. Cem Concr Res 2010;40:956–65.
[12] Tomar V. Modeling of dynamic fracture and damage in two-dimensional trabecular bone microstructures using the cohesive finite element method. J Biomech Engng 2008;130:1–10.
[13] Ural A, Vashishth D. Cohesive finite element modeling of age-related toughness loss in human cortical bone. J Biomech 2006;39:2974–82.
[14] Zhang ZJ, Zhang P, Li LL, Zhang ZF. Fatigue cracking at twin boundaries: effects of crystallographic orientation and stacking fault energy. Acta Mater 2012;60:3113–27.
[15] Song SH, Paulino GH, Buttlar WG. A bilinear cohesive zone model tailored for fracture of asphalt concrete considering viscoelastic bulk material. Engng Fract Mech 2006;73:2829–48.
[16] Hui CY, Ruina A, Long R, Jagota A. Cohesive zone models and fracture. J Adhes 2011;87:1–52.
[17] Park K, Paulino GH. Cohesive zone models: a critical review of traction–separation relationships across fracture surfaces. Appl Mech Rev 2013;64(060802):1–20.
[18] Tvergaard V. Material failure by void growth to coalescence. Adv Appl Mech 1990;27:83–151.
[19] Needleman A. An analysis of tensile decohesion along an interface. J Mech Phys Solids 1990;38:289–324.
[20] Xu XP, Needleman A. Void nucleation by inclusion debonding in a crystal matrix. Model Simul Mater Sci Engng 1993;1:111–32.
[21] Park K, Paulino GH, Roesler JR. A unified potential-based cohesive model of mixed-mode fracture. J Mech Phys Solids 2009;57:891–908.
[22] Balay S, Gropp WD, McInnes LC, Smith BF. Efficient management of parallelism in object-oriented numerical software libraries. In: Mordern Software Tools for Scientific Computing, Birkhäuser, Boston; 1997. p. 163–202.
[23] Balay S, Brown J, Buschelman K, Eijkhout V, Gropp WD, Kaushik D, et al. PETSc Users Manual; 2010.
[24] Balay S, Brown J, Buschelman K, Gropp WD, Kaushik D, Knepley MG, et al. PETSc Web Page; 2011.
[25] Alfano M, Furgiuele F, Lubineau G, Paulino GH. Simulation of debonding in Al/epoxy T-peel joints using a potential-based cohesive zone model. Procedia Engng 2011;10:1760–5.
[26] Alfano M, Lubineau G, Furgiuele F, Paulino GH. On the enhancement of bond toughness for Al/epoxy T-peel joints with laser treated substrates. Int J Fract 2011;171:139–50.

[27] Rice JR. Mathematical Analysis in the Mechanics of Fracture. In: Liebowitz H, editor. Fract an adv treatise, vol. 2. Academic Press; 1968. p. 191–311.
[28] ASTM. Standard test method for mixed mode I–mode II interlaminar fracture toughness of unidirectional fiber reinforced polymer matrix composites. ASTM D 6671/D 6671M; 2006.
[29] Reeder JR, Crews Jr JH. Mixed-mode bending method for delamination testing. AIAA J 1990;28:1270–6.
[30] Mi Y, Crisfield MA, Davies GAO, Hellweg HB. Progressive delamination using interface elements. J Compos Mater 1998;32:1246–72.
[31] Ratcliffe JG. Characterization of the edge crack torsion (ECT) test for mode III fracture toughness measurement of laminated composites. NASA Technical Memorandum, NASA/TM-2004-213269; 2004.
[32] Krueger R, O'Brien T. Analysis of flexure tests for transverse tensile strength characterization of unidirectional composites. J Compos Technol Res 2003;25:11231.
[33] Igi S, Kawaguchi S, Suzuki N. Running ductile fracture analysis for X80 pipeline in JGA burst tests. In: Pipeline technol conf, Ostend, Belgium; 2009.
[34] Nonn A, Kalwa C. Modeling of damage behavior of high strength pipeline steel. In: 18th Eur conf fract, Dresden, Germany; 2010.
[35] ASTM. Standard test method for drop-weight tear tests of ferritic steel. ASTM E436; 2008.
[36] API. Recommended practice for conducting drop weight tear tests on line pipe. API RP 5L3; 1996.
[37] EN. Metallic materials – drop weight tear test. EN 10274; 1999.
[38] Nègre P, Steglich D, Brocks W. Crack extension at an interface: prediction of fracture toughness and simulation of crack path deviation. Int J Fract 2005;134:209–29.
[39] Roy YA, Dodds RH. Simulation of ductile crack growth in thin aluminum panels using 3-D surface cohesive elements. Int J Fract 2001;110:21–45.
[40] Scheider I, Schödel M, Brocks W, Schönfeld W. Crack propagation analyses with CTOA and cohesive model: comparison and experimental validation. Engng Fract Mech 2006;73:252–63.
[41] Raj R, Ashby MF. Intergranular fracture at elevated temperatures. Acta Metall 1975;23:653–66.
[42] Groeber M, Ghosh S, Uchic MD, Dimiduk DM. A framework for automated analysis and simulation of 3D polycrystalline microstructures. Part 1: statistical characterization. Acta Mater 2008;56:1257–73.
[43] Groeber M, Ghosh S, Uchic MD, Dimiduk DM. A framework for automated analysis and simulation of 3D polycrystalline microstructures. Part 2: synthetic structure generation. Acta Mater 2008;56:1274–87.